

# Observations of Seasonal Upwelling and Downwelling in the Beaufort Sea Mediated by Sea Ice

GIANLUCA MENEHELLO AND JOHN MARSHALL

*Department of Earth, Atmospheric and Planetary Sciences, Massachusetts Institute of Technology, Cambridge, Massachusetts*

MARY-LOUISE TIMMERMANS

*Department of Geology and Geophysics, Yale University, New Haven, Connecticut*

JEFFERY SCOTT

*Department of Earth, Atmospheric and Planetary Sciences, Massachusetts Institute of Technology, Cambridge, Massachusetts*

(Manuscript received 16 September 2017, in final form 14 December 2017)

## ABSTRACT

We present observational estimates of Ekman pumping in the Beaufort Gyre region. Averaged over the Canada Basin, the results show a 2003–14 average of  $2.3 \text{ m yr}^{-1}$  downward with strong seasonal and interannual variability superimposed: monthly and yearly means range from  $30 \text{ m yr}^{-1}$  downward to  $10 \text{ m yr}^{-1}$  upward. A clear, seasonal cycle is evident with intense downwelling in autumn and upwelling during the winter months, despite the wind forcing being downwelling favorable year-round. Wintertime upwelling is associated with friction between the large-scale Beaufort Gyre ocean circulation and the surface ice pack and contrasts with previous estimates of yearlong downwelling; as a consequence, the yearly cumulative Ekman pumping over the gyre is significantly reduced. The spatial distribution of Ekman pumping is also modified, with the Beaufort Gyre region showing alternating, moderate upwelling and downwelling, while a more intense, yearlong downwelling averaging  $18 \text{ m yr}^{-1}$  is identified in the northern Chukchi Sea region. Implications of the results for understanding Arctic Ocean dynamics and change are discussed.

## 1. Introduction

Ekman pumping plays a central role in the generation and maintenance of the Beaufort Gyre (BG), the largest freshwater reservoir in the Arctic (Proshutinsky et al. 2009). The pumping rates are proportional to the curl of the surface stress, with the stress being a combination of the winds' effect over the open ocean, and of the ice—itsself driven by the wind—moving over the ice-covered ocean.

Most estimates of Ekman pumping assume that surface ocean geostrophic currents can be neglected (Yang 2006, 2009; Ma et al. 2017) or focus on the summer season when ice can be considered in free drift (McPhee 2013). The resulting Ekman pumping field, driven by anticyclonic winds and ice drift associated with the highly variable but persistent high-pressure system over the Beaufort region, is characterized by year-long

downwelling, modulated by a seasonal cycle in intensity but not in sign (Proshutinsky et al. 2009). Therefore, it is assumed that the gyre is continuously inflated with freshwater, which can be released by baroclinic instability-generated eddies (Manucharyan and Spall 2016; Manucharyan et al. 2016; Meneghello et al. 2017). The limit case in which Ekman pumping is exactly balanced by eddy-induced upwelling is exploited in Meneghello et al. (2017) to place a constraint on the magnitude of the mesoscale eddy diffusivity.

Hydrographic and satellite-based observations suggest that surface geostrophic currents have increased dramatically over the past decade, consistent with the observed increase of freshwater content in the Beaufort Gyre region (Proshutinsky et al. 2009; MCPhee 2013) or the equivalent doming of the dynamic ocean topography or geopotential height (Armitage et al. 2016, 2017). Geostrophic currents of the order of  $3 \text{ cm s}^{-1}$  and up to  $10 \text{ cm s}^{-1}$  or more in the southern BG (Armitage et al. 2017) cannot be neglected compared to ice velocities of

---

*Corresponding author:* Gianluca Meneghello, gianluca.meneghello@gmail.com

order 5 to  $10 \text{ cm s}^{-1}$ . This is particularly true during winter in regions where internal ice stresses prevent the pack from freely moving in response to wind forcing. In this case, the friction between the anticyclonic surface ocean geostrophic flow and a relatively stationary sea ice pack gives rise to upwelling (in opposition to downwelling that would arise for the same wind forcing in the absence of sea ice). Indeed, in situ observations from moorings and ice-tethered profilers (ITPs) show current speeds that can be larger than the ice speed, as detailed in the [appendix](#) (and [Fig. A1](#)).

Numerical studies ([Martin and Gerdes 2007](#); [Martin et al. 2014, 2016](#)) implicitly take into account the surface ocean current but have not emphasized the implications for the Ekman pumping field itself or teased apart the controlling processes. Instead, they often focus on characterization of sea ice drift, the surface stress, and the effect of varying drag coefficients. Using observational datasets, we showed in [Meneghello et al. \(2017\)](#) how the inclusion of the interaction between the ice and geostrophic current associated with the Beaufort Gyre significantly changes the annual-mean Ekman pumping. A detailed analysis of the updated Ekman pumping is the focus of the current study.

In this paper, we analyze observations spanning the period 2003 to 2014 to discern how the complex relationships between winds, a temporally and spatially varying sea ice pack, and surface ocean geostrophic flows influence Ekman upwelling and downwelling in the central Beaufort Gyre region (BGR) and margins. In previous studies ([Yang 2006, 2009](#); [McPhee 2013](#)), the central gyre has been discussed in a broad sense without regard for topographic boundaries; the essential dynamics at its margins are often ignored. Here, we further explore the significant regional patterns of the Ekman pumping field and describe their importance to the gyre as a whole.

The paper is organized as follows: We begin in [section 2](#) by outlining the methods used to compute Ekman pumping rates; our approach is similar to the one used by [Yang \(2006, 2009\)](#), with the main difference being the addition of the geostrophic current introduced in [Meneghello et al. \(2017\)](#). In [section 3](#), we present estimates of the Ekman pumping field; we plot the time series of Ekman pumping averaged over the BGR, bounded by  $70.5^\circ$  to  $80.5^\circ\text{N}$  and  $130^\circ$  to  $170^\circ\text{W}$ , and including only regions having a depth greater than 300 m ([Proshutinsky et al. 2009](#)). We follow in [section 4](#) with a discussion of the spatial distribution of Ekman pumping in the BGR, additionally focusing attention on two smaller regions of particular interest in the south of the Canada Basin (BGS) and in the northern Chukchi Sea region (BGC). Results are discussed in [section 5](#), where

we clarify the effect of the interaction of surface–ocean geostrophic currents with the sea ice pack and implications to mechanisms controlling the time-dependent buoyancy budget of the Beaufort Gyre in the presence of seasonal sea ice.

## 2. Methods

Four datasets are combined to estimate the surface ocean stress  $\tau$  and Ekman pumping  $w_{\text{Ek}}$ : (i) sea ice concentration  $\alpha$  from *Nimbus-7* SMMR and DMSP SSM/I–SSMIS passive microwave data, version 1 ([Cavalieri et al. 1996](#)); (ii) sea ice velocity  $\mathbf{u}_i$  from the Polar Pathfinder daily 25-km Equal-Area Scalable Earth Grid (EASE-Grid) sea ice motion vectors, version 3 ([Tschudi et al. 2016](#)); (iii) geostrophic currents  $\mathbf{u}_g$  computed from dynamic ocean topography ([Armitage et al. 2016, 2017](#)); and (iv) 10-m wind  $\mathbf{u}_a$  from the NCEP–NCAR Reanalysis 1 ([Kalnay et al. 1996](#)). The four different datasets, defined on different grids, are interpolated on a common EASE 25-km polar stereographic equal area grid, which is the native grid for the ice velocity. All datasets are available in at least daily resolution, with the exception of dynamic ocean topography having monthly resolution; to produce daily values, we arbitrarily assign the available fields to the fifteenth of the corresponding month and linearly interpolate. Changing the day of the month does not significantly affect our results, and submonthly variability of the geostrophic current is presumed to be small. The 2003–14 climatology of these four variables is summarized in [Fig. 1](#), while variability in time is summarized by their mean values over the BGR ([Fig. 2a](#)).

The high pressure system at the origin of the gyre is evident in the 10-m wind field ([Fig. 1a](#)), where the anticyclonic flow is centered at approximately  $76^\circ\text{N}$  and  $145^\circ\text{W}$ ; stronger winds, of order  $2.5 \text{ m s}^{-1}$ , are in the southwestern BGR (the region indicated by a solid black line), while winds are weaker ( $\sim 1 \text{ m s}^{-1}$  or less) in the northern BGR. Sea ice drift and surface–ocean geostrophic flow ([Figs. 1b and 1c](#), respectively) also show anticyclonic circulation patterns with the strongest speeds ( $\sim 5 \text{ cm s}^{-1}$ ) in the southwest and slowest speeds in the north.

Time series of mean values over the BGR ([Fig. 2a](#)) indicate a seasonal cycle in the four datasets: ice areal coverage reaches a minimum between 20% and 40% every late summer, with the extreme low in 2012 when the BG was close to ice free. Wind speeds tend to peak in late summer/early fall, when sea ice drift speeds are also fastest. The surface ocean current shows maximum speeds during late fall, peaking at about twice the characteristic speed of the first part of the year; of particular note is its

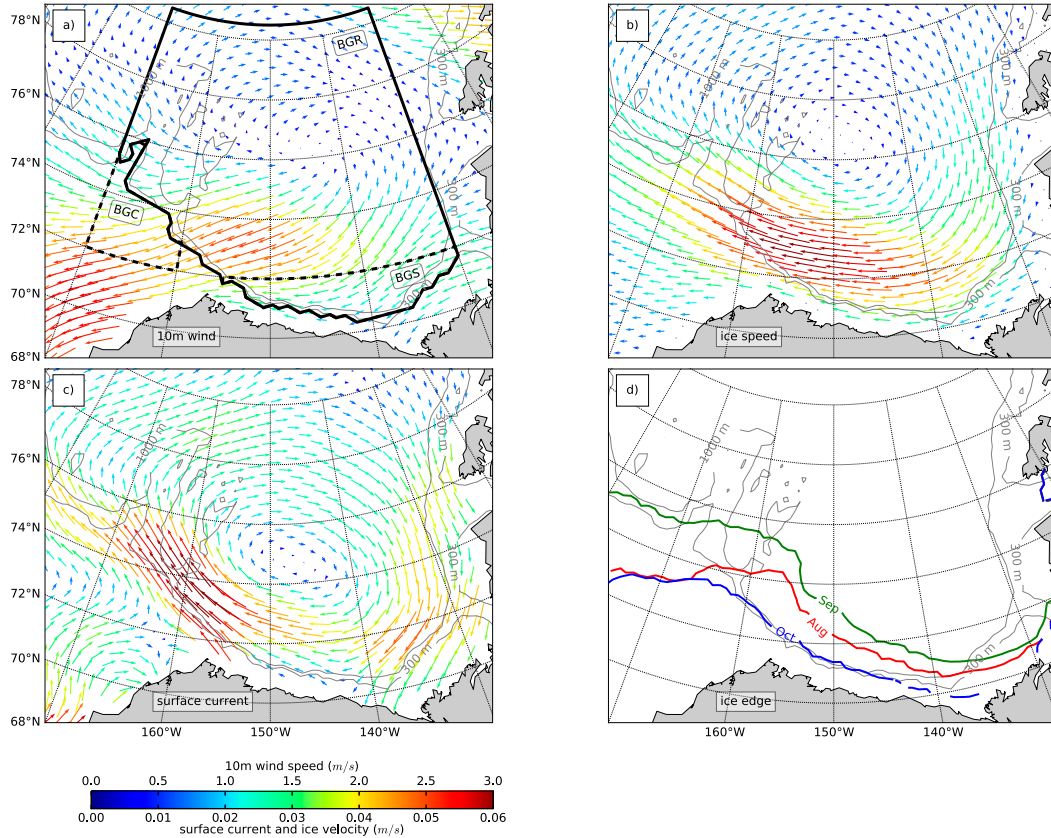


FIG. 1. The 12-yr means of the four datasets combined to produce estimates of the Ekman pumping field: (a) 10-m wind, (b) ice velocity, (c) surface geostrophic current, and (d) ice edge (15% ice concentration) for August, September, and October (the ice concentration is larger than 15% everywhere for the rest of the year). The thick black line delimits the BGR, while dashed lines delimit the northern Chukchi Sea region (BGC) and the region south of the Canada Basin (BGS)—see section 4.

increase in the second part of 2007 (and sustained for several years following).

Starting from the four datasets described above, we use the same approach used in Meneghello et al. (2017) and compute the daily surface–ocean stress  $\tau$  as a combination of ice–ocean and air–ocean surface stresses, each estimated using a quadratic drag law with fixed drag coefficients ( $C_{Di} = 0.0055$ ;  $C_{Da} = 0.00125$ ) and weighted by the observed local ice concentration  $\alpha$ :

$$\tau = \alpha \underbrace{\rho C_{Di} |\mathbf{u}_{rel}| (\mathbf{u}_{rel})}_{\tau_i} + (1 - \alpha) \underbrace{\rho_a C_{Da} |\mathbf{u}_a| (\mathbf{u}_a)}_{\tau_a}, \quad (1)$$

where the ice–ocean relative velocity  $\mathbf{u}_{rel}$  may be written in terms of the ice velocity  $\mathbf{u}_i$ , the surface geostrophic velocity  $\mathbf{u}_g$ , and the Ekman velocity  $\mathbf{u}_e$  as  $\mathbf{u}_{rel} = \mathbf{u}_i - (\mathbf{u}_g + \mathbf{u}_e)$ . The water and air density are taken as  $\rho = 1027.5 \text{ kg m}^{-3}$  and  $\rho_a = 1.25 \text{ kg m}^{-3}$ , respectively.

Our estimate of the surface ocean current differs from, for example, Yang (2006, 2009) in two key ways:

First, we use the Ekman velocity at the surface (rotated  $45^\circ$  to the right of the surface stress) in place of the mean Ekman transport velocity ( $90^\circ$  from the surface stress); thus,  $\mathbf{u}_e = \tau \sqrt{2} e^{-i(\pi/4)} / (f \rho D_e)$ , with  $D_e = 20 \text{ m}$  (Yang 2006). Second, and more importantly, we include the surface geostrophic current  $\mathbf{u}_g$  inferred from dynamic ocean topography (McPhee 2013; Armitage et al. 2016, 2017).

### 3. Ekman pumping estimates: Integral measures

The Ekman pumping rate  $w_{EK} = (\nabla \times \tau) / (\rho f)$  is computed, making use of the daily stress fields obtained as described above, where  $f$  is the Coriolis parameter. We first focus on integral measures averaged over the BGR, summarized in Fig. 2b. Over the 12-yr period 2003–14, Ekman convergence (solid black curve; negative is downward) results in an average downwelling  $w_{EK}$  of  $2.3 \text{ m yr}^{-1}$  to be compared with an average of almost  $10 \text{ m yr}^{-1}$  if the geostrophic current is neglected (dashed black). By comparison, in the scenario of a completely

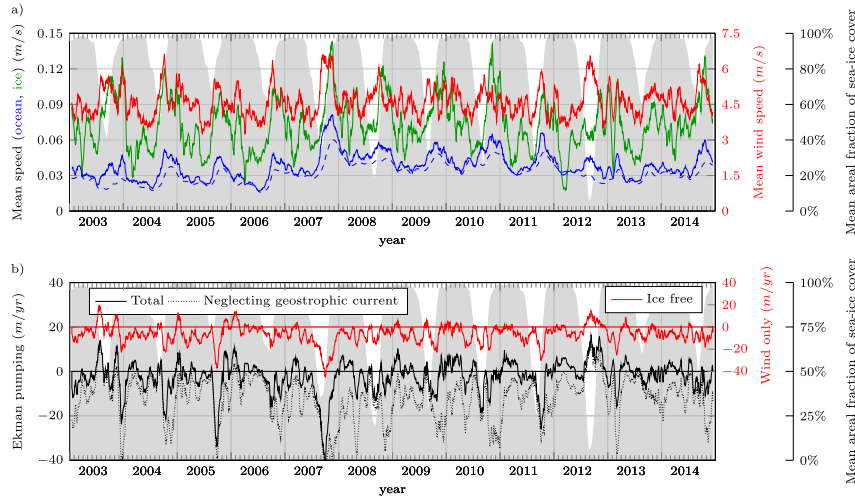


FIG. 2. (a) The 30-day running mean of 10-m wind speed  $u_a$  (red), ice speed  $u_i$  (green), surface geostrophic current speed  $u_g$  (dashed blue), and surface ocean speed  $u_g + u_e$  (solid blue). (b) The 30-day running-mean Ekman pumping  $w_{\text{Ek}}$  (solid black), Ekman pumping in the absence of geostrophic current  $w_{i0}$  (dotted black), and Ekman pumping for a completely ice-free BGR  $w_A$  (red, note axes on the right). Gray areas in both panels show ice concentration  $\alpha$ .

ice-free BGR, the wind-driven downwelling would be  $6.3 \text{ m yr}^{-1}$  (solid red).

To better understand the role of the winds, sea ice, and ocean geostrophic currents, we additionally compute the contribution of the geostrophic current to the ice stress as

$$\boldsymbol{\tau}_{ig} = \boldsymbol{\tau}_i - \boldsymbol{\tau}_{i0}, \quad (2)$$

where  $\boldsymbol{\tau}_{i0}$  is the ice–ocean stress neglecting the geostrophic current, that is, computed by setting  $\mathbf{u}_g = 0$  in Eq. (1). Accordingly, we define the Ekman pumping associated with each component as

$$\begin{aligned} w_a &= \frac{\nabla \times [(1 - \alpha)\boldsymbol{\tau}_a]}{\rho f}, & w_i &= \frac{\nabla \times (\alpha\boldsymbol{\tau}_i)}{\rho f}, \\ w_{i0} &= \frac{\nabla \times (\alpha\boldsymbol{\tau}_{i0})}{\rho f}, & w_{ig} &= \frac{\nabla \times (\alpha\boldsymbol{\tau}_{ig})}{\rho f}, \end{aligned} \quad (3)$$

so that the total Ekman pumping can be written as  $w_{\text{Ek}} = (\nabla \times \boldsymbol{\tau})/(\rho f) = w_a + w_i = w_a + w_{i0} + w_{ig}$ . As a measure of the atmospheric forcing, we additionally define

$$w_A = \frac{\nabla \times \boldsymbol{\tau}_a}{\rho f} \quad (4)$$

as the Ekman pumping that would be realized in a completely ice-free BGR.

The area-averaged Ekman pumping time series (30-day running means of daily values; Fig. 2b) shows how both the atmospheric forcing  $w_A$  (red) and Ekman pumping computed neglecting the geostrophic current  $w_a + w_{i0}$  (dotted black) are almost always downwelling

favorable. In contrast, the actual pumping  $w_{\text{Ek}}$  (solid black) has extensive periods of upwelling in the winter of each year corresponding to periods when the ice concentration is elevated (gray areas) and strong downwelling in late summer and autumn, when ice concentration is low.

The role of each component in determining the total upwelling or downwelling in the BGR is made clearer in the monthly and yearly area averages (Fig. 3) of  $w_{\text{Ek}}$  (black bars) and its three components  $w_a$  (red bars),  $w_{i0}$ , and  $w_{ig}$  (green and blue bars respectively). We additionally plot  $w_A$  (red and white circles),  $w_a + w_{i0}$  (red green marks), and the ice concentration (gray circles) as well as the ratio

$$\gamma = \frac{|w_{ig}|}{|w_a| + |w_{i0}| + |w_{ig}|} \quad (5)$$

as a metric of the importance of the geostrophic current relative to the total Ekman pumping (black line).

A seasonal cycle is evident in the monthly climatology of  $w_{\text{Ek}}$  (black bars; Fig. 3a): upwelling in January to March is followed by increasing downwelling over the rest of the year, reaching an October downwelling maximum of slightly less than  $10 \text{ m yr}^{-1}$ , driven by strong wind stress curl forcing (red and white circles) acting on a largely ice-free BGR (gray circles). Downwelling markedly decreases in November and December because of the combined effect of weaker wind stress curl and high ice concentration. Strong downwelling in the low ice concentration months of August to October is driven by direct air–ocean wind stress curl (red bars) and closely follows the hypothetical downwelling result if the BGR was ice free

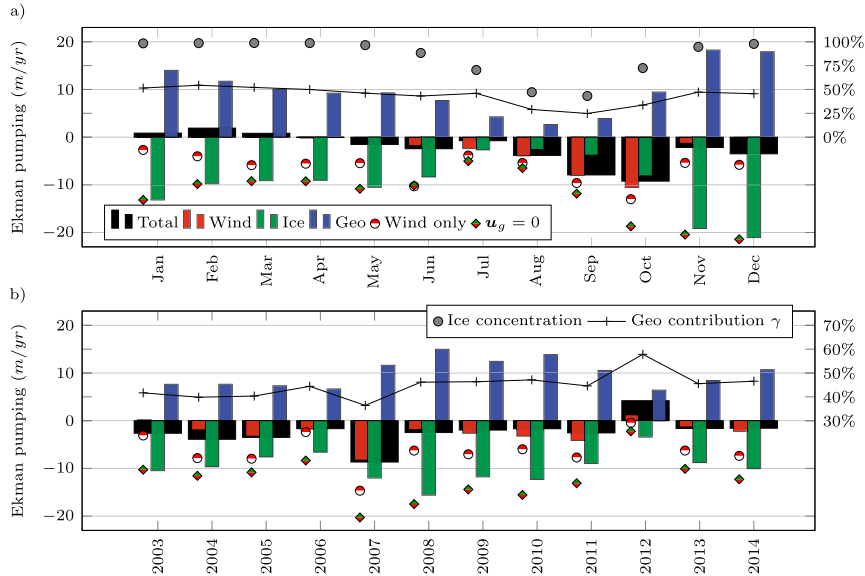


FIG. 3. Area-averaged values over the BGR of (a) monthly and (b) yearly climatologies of Ekman pumping (black bars) and its three main components:  $w_a$  (red bars; the pumping over the open ocean),  $w_{i0}$  (green bars; the pumping in the ice-covered ocean in the absence of a geostrophic current), and  $w_{ig}$  (blue bars; modification of underice pumping caused by the geostrophic ocean current). The red and green diamonds give the total Ekman pumping  $w_a + w_{i0}$  in the absence of the ocean geostrophic contribution, that is, the sum of the red and green bars. The red and white circles give the wind-driven Ekman pumping  $w_A$  in a completely ice-free BGR, a proxy of the atmospheric forcing over the entire region. The pumping scale is on the left. The thin black line is a measure of the importance of geostrophic currents given by Eq. (5) (scale on the right-hand side). The gray circles in (a) indicate the ice concentration  $\alpha$  (scale on the right).

(red and white circles); during these months, the effects of ice and geostrophic currents are relatively minor. During the rest of the year, when ice cover is extensive, direct air-ocean stress plays a minor role, and stresses are predominantly mediated by ice cover. The importance of the geostrophic current on the total Ekman pumping, as measured by the ratio  $\gamma$  [Eq. (5), black line], closely follows the ice concentration: when the BGR is completely ice covered and internal stresses are higher (January to March), the surface ocean geostrophic current is faster than sea ice drift, resulting in net upwelling. Indeed, while the ice effect (green bars) is always downwelling favorable, the effect of the geostrophic current (blue bars) is consistently upwelling and of the same order of magnitude.

The yearly climatology (Fig. 3b) presents a similar range of total Ekman pumping values (black bars) between years and closely follows the variability of the wind stress curl acting directly on the ice-free parts of the ocean (red bars), with the ice and geostrophic current effects approximately canceling one another. Notable exceptions are in 2003 and 2004, when downwelling is mostly driven by ice (green bars) flowing over a slower geostrophic current (blue bars), and in 2012, when a fast geostrophic

current and cyclonic winds (in the opposite sense to the geostrophic ocean flow) both contribute to upwelling. We remark that 2012 is unusual in having a strong upwelling-favorable atmospheric forcing during the second part of the year, possibly related to the Great Arctic Cyclone described by Simmonds and Rudeva (2012).

#### 4. Ekman pumping estimates: Spatial patterns

To better understand the spatial distribution of upwelling and downwelling in the Beaufort Gyre region, we plot monthly and yearly climatological maps of Ekman pumping (Figs. 4 and 5, respectively).

We additionally repeat the decomposition of the total Ekman pumping (cf. Fig. 3) for two smaller regions: (i) the BGC, delimited by  $72^\circ$  to  $76^\circ\text{N}$ ,  $170^\circ$  to  $160^\circ\text{W}$ , and including only regions shallower than 300m (thus outside the BGR), and (ii) the BGS, covering the portion of the BGR south of the  $72^\circ\text{N}$  parallel (see dashed lines and labels in Fig. 1a).

During the first 4 months of the year [January–April (JFMA)], a broad region of upwelling is visible in the BGR, particularly toward the southern sector, with local

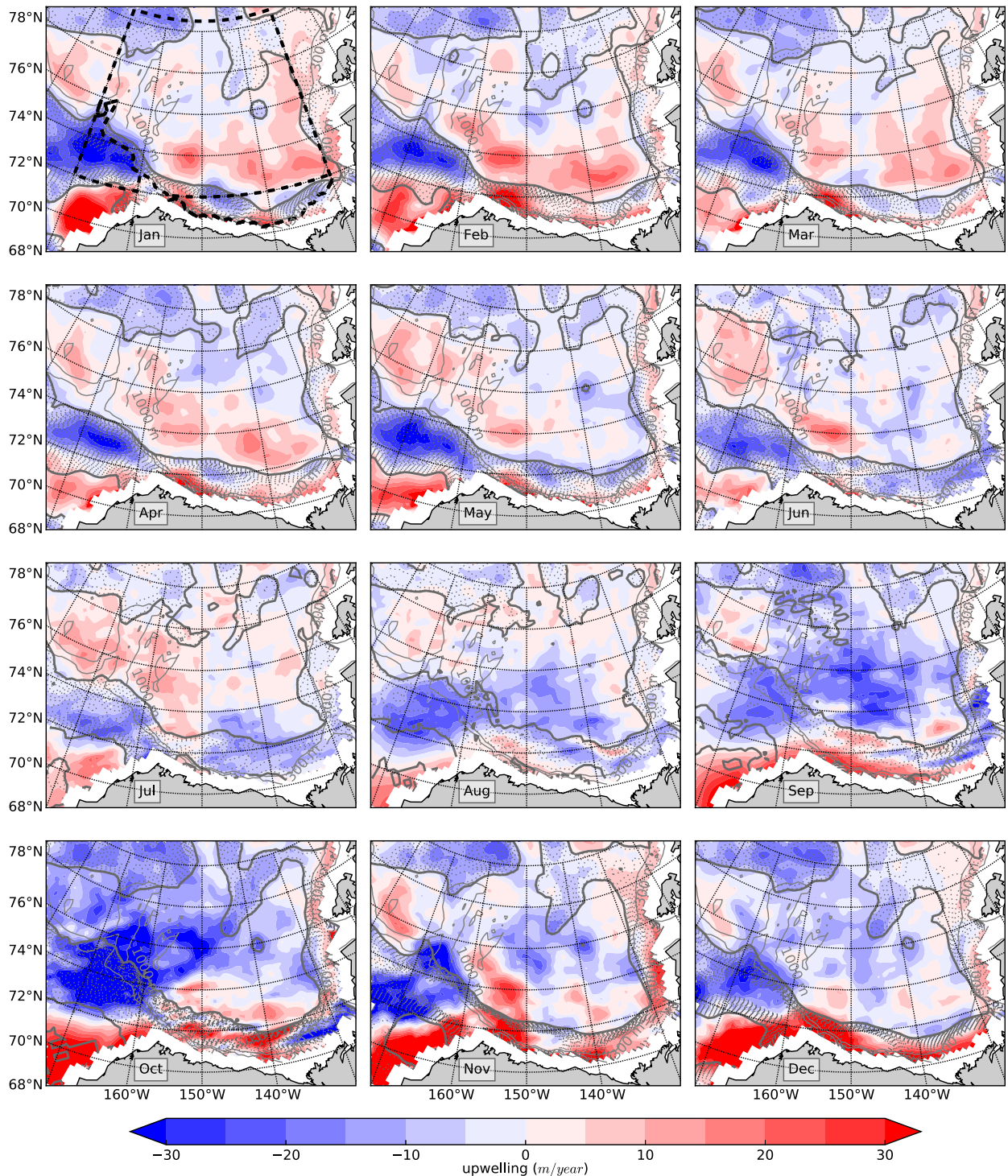


FIG. 4. Monthly climatology of Ekman pumping field ( $\text{m yr}^{-1}$ ). The black dashed lines denotes the limits of the BGR, BGS, and BGC regions (see Fig. 1). Gray thick lines mark the location where the geostrophic current component contribution is zero. Interior to this line, the geostrophic current gives an upwelling contribution; outside (stippled regions), it enhances downwelling.

upwelling rates as high as 25 to 30  $\text{m yr}^{-1}$  (Fig. 4). In the following 4 months [May–August (MJJA)], the intensity and extension of the upwelling region decreases; by

September, downwelling dominates over most of the BGR. For all months, a marked region of downwelling persists to the southwest of the BGR in the northern

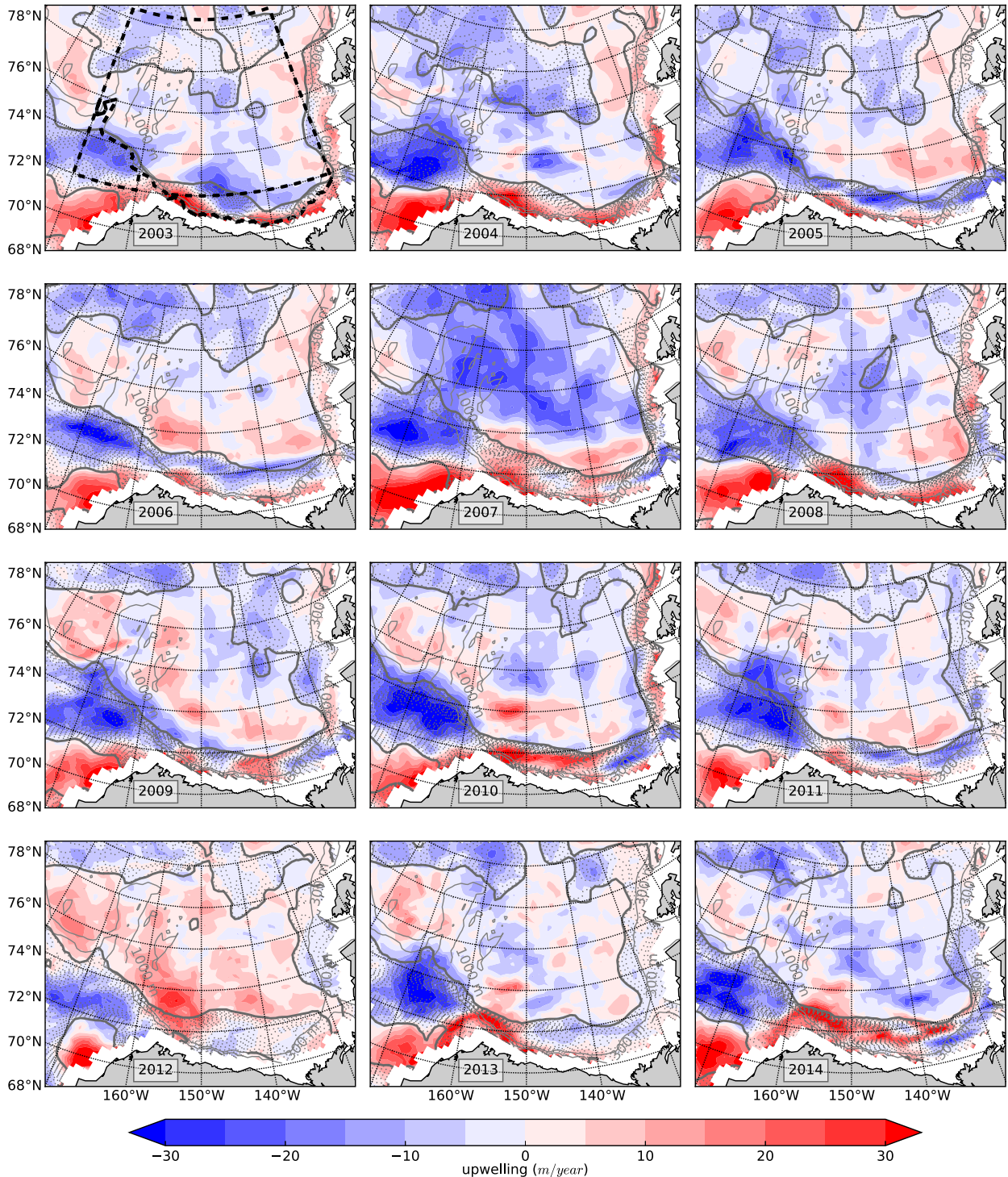


FIG. 5. Yearly climatology of Ekman pumping field ( $\text{m yr}^{-1}$ ). The black dashed line denotes the limits of the BGR, BGS, and BGC regions (see Fig. 1). Gray thick lines mark the location where the geostrophic current component contribution is zero. Interior to this line, the geostrophic current gives an upwelling contribution; outside (stippled regions), it enhances downwelling.

Chukchi Sea (in the region we denote BGC). Downwelling in this region intensifies in fall, with October showing downwelling rates in excess of  $30 \text{ m yr}^{-1}$ .

An indication of the role of the geostrophic current in shaping the spatial distribution of Ekman pumping can be inferred by the gray thick line (Fig. 4). In the region

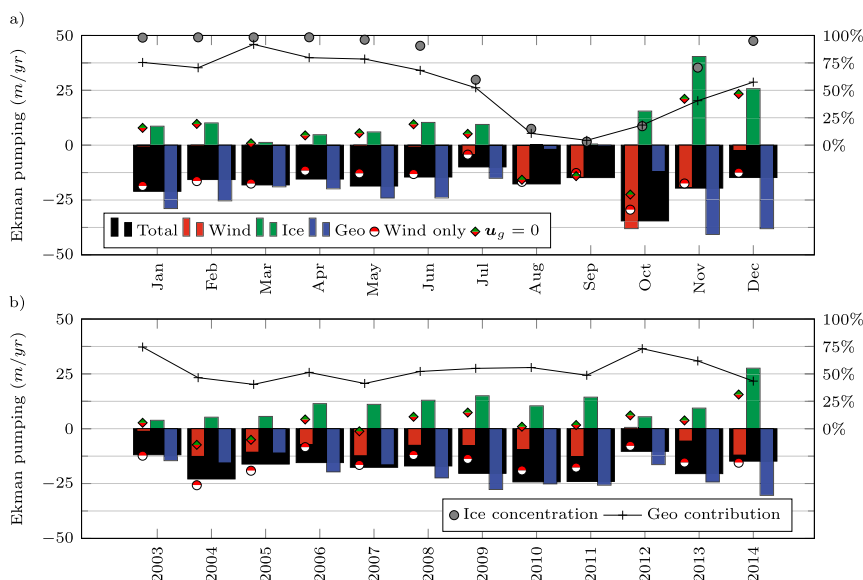


FIG. 6. As in Fig. 3, but for the BGC.

interior to this line, the geostrophic current reduces the ice-driven downwelling and sometimes gives rise to a net upwelling [i.e., January–March (JFM)]. In contrast, downwelling is enhanced by the presence of the geostrophic current outside the gray curve (stippled areas).

Yearly averaged maps of Ekman pumping (Fig. 5) show weak Ekman downwelling and upwelling over most of the BGR. Notable exceptions to this general pattern are the years 2007 and 2012. In 2007, strong and persistent downwelling-favorable wind stress curl (Fig. 2b, red curve), in conjunction with a record low sea ice extent, resulted in anomalously intense downwelling extending over most of the Beaufort Gyre, with the exception of coastal upwelling in the south (Fig. 5). As a consequence, the latter part of 2007 saw an increase in downwelling and freshwater content (Armitage et al. 2016, their Fig. 6). The related stronger currents and larger ice velocities persisted over the next 5 years until 2012 (see Fig. 2a, blue dashed line; Armitage et al. 2016, 2017; Kwok et al. 2013). In contrast, 2012 was characterized by extended upwelling driven by summer cyclonic winds (see Fig. 2b, red curve; Simmonds and Rudeva 2012) in the presence of anomalously low sea ice concentration. The record low ice extent can be explained by wind-driven Ekman divergence acting on an ice cover that had significantly thinned after the 2007/08 record ice low, when most multiyear ice was lost (Giles et al. 2008). The resulting deflation of the gyre is evident in the decrease of the geostrophic current intensity, which returns to its pre-2007 level for at least the following 2 years.

Analysis of the varying distribution of Ekman pumping (Figs. 4, 5) indicates strong, continuous downwelling in the

BGC and strong Ekman pumping of variable sign in the southern part of the BGR (the region denoted BGS).

A detailed analysis of the BGC and BGS regions is provided in Figs. 6 and 7, respectively. The BGC region (Fig. 6) is characterized by strong, year-long downwelling averaging  $17.9 \text{ m yr}^{-1}$  over the 12-yr period. Prevailing easterlies tend to be consistently stronger here compared to anywhere else in the basin (see Fig. 1a) and decay toward the north leading to the highest values of horizontal shear and downwelling in this region. The upwelling associated with the positive ice velocity curl (Fig. 1c) is offset by the contribution of the ocean geostrophic flow, which is swiftest along the lateral density front approximately coincident with the 100-m isobath (Timmermans et al. 2017; Fig. 1b).

In contrast, in the BGS region (Fig. 7) winds and ice velocity increasing in intensity away from the coast results in a 2003–14 mean upwelling of  $2.3 \text{ m yr}^{-1}$ . Wind-driven downwelling is apparent only in the months of June, July, and August, when ice cover is reduced and there is negligible decay of northeasterly winds toward the coast.

It is instructive to compare the relative importance of the total vertical Ekman flux (in this case, upwelling plus downwelling) in each of the different regions: BGR, BGS, and BGC. Table 1 summarizes the surface area, 2003–14 mean Ekman pumping  $w_{\text{EK}}$ , and the total corresponding vertical flux for each region. Because of the large downwelling, the vertical flux in the BGC region is approximately two-thirds of that in the BGR, despite the former having only one-tenth of the surface area of the latter. We further point out that downwelling in the BGC is sustained

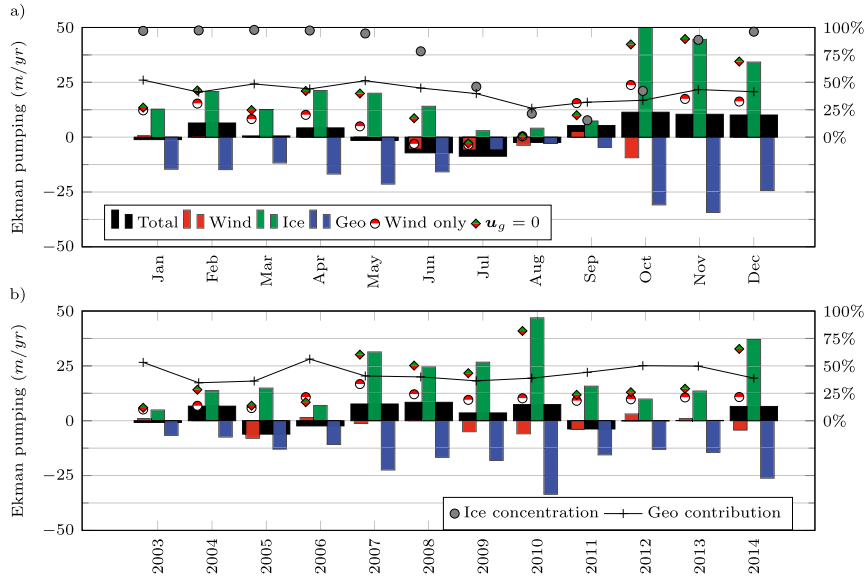


FIG. 7. As in Fig. 3, but for the BGS.

(seasonally and interannually), and it has been shown to be a region of key importance for ventilation of the interior Beaufort Gyre; Timmermans et al. (2017) estimate that about one-fifth of the Beaufort Gyre warm halocline could be renewed by subduction from this region in one summer.

5. Conclusions and discussion

Observational estimates of Ekman pumping in the BGR show a weak 12-yr average Ekman downwelling of order  $-2.3 \text{ m yr}^{-1}$ , with strong seasonal and interannual variability: monthly and yearly mean Ekman pumping range from  $-30 \text{ m yr}^{-1}$  to up to  $10 \text{ m yr}^{-1}$ . A clear seasonal cycle is visible: the Beaufort Gyre is driven by upwelling during the winter months and intense downwelling in autumn. Our results contrast with previous estimates showing year-long downwelling (Yang 2006, 2009; Ma et al. 2017) and reduce by a factor of 4 or more the yearly cumulative Ekman pumping in the gyre; the main reason for this difference is our inclusion of the effect of the geostrophic current, which flows in the same direction as the prevailing winds and sea ice drift. Such ocean-ice interaction acts as a strong negative feedback on the response of the gyre to changing winds and could have potential implications for the wider Arctic. In particular, strong ocean currents (larger than  $10 \text{ cm s}^{-1}$ ; Armitage et al. 2017) off the east coast of Greenland have the potential to modulate Ekman downwelling estimates by both Yang (2006, 2009) and Ma et al. (2017). Furthermore, we have identified a region of strong, persistent downwelling (the BGC region) that accounts for a significant fraction of the total Ekman transport in the entire Canada Basin. The precise influence of the

BGC region on Beaufort Gyre dynamics and stability, and heat and freshwater content, remains to be tested.

In the larger BGR, the seasonal alternation of wind-driven downwelling and geostrophic current-driven upwelling suggests a new possible mechanism in the regulation of Beaufort Gyre intensity.

Recent numerical and observational studies (Manucharyan and Spall 2016; Manucharyan et al. 2016, 2017; Meneghello et al. 2017) analyze the Beaufort Gyre under the assumption of persistent downwelling. In this limit, an intense baroclinic eddy field is required to arrest the spinup and freshwater accumulation (steepening of the isopycnals) of the gyre. Horizontal eddy diffusivity estimates for the Beaufort Gyre are around  $K \approx 500 \text{ m}^2 \text{ s}^{-1}$  (Manucharyan and Spall 2016; Manucharyan et al. 2016; Meneghello et al. 2017), suggesting freshwater release takes place on a diffusive time scale of  $L^2/K \approx 15 \text{ yr}$  if the characteristic lateral scale of the gyre is  $L = 500 \text{ km}$ .

Instead, the observations presented here suggest that both the buildup and release of freshwater could be at least partially mediated by winter Ekman upwelling. More research is required to discern the interplay between

TABLE 1. The 2003–14 areal-mean Ekman pumping  $w_{\text{EK}}$  and vertical flux for the BGR, BGC, and BGS regions, where negative implies downward. Vertical flux is the product of the first two columns ( $1 \text{ Sv} \equiv 10^6 \text{ m}^3 \text{ s}^{-1}$ ).

	Surface ( $\text{km}^2$ )	$w_{\text{EK}}$ ( $\text{m yr}^{-1}$ )	Vertical flux (Sv)
BGR	989 375	-2.3	-0.072
BGC	85 000	-17.9	-0.048
BGS	95 000	2.3	0.007

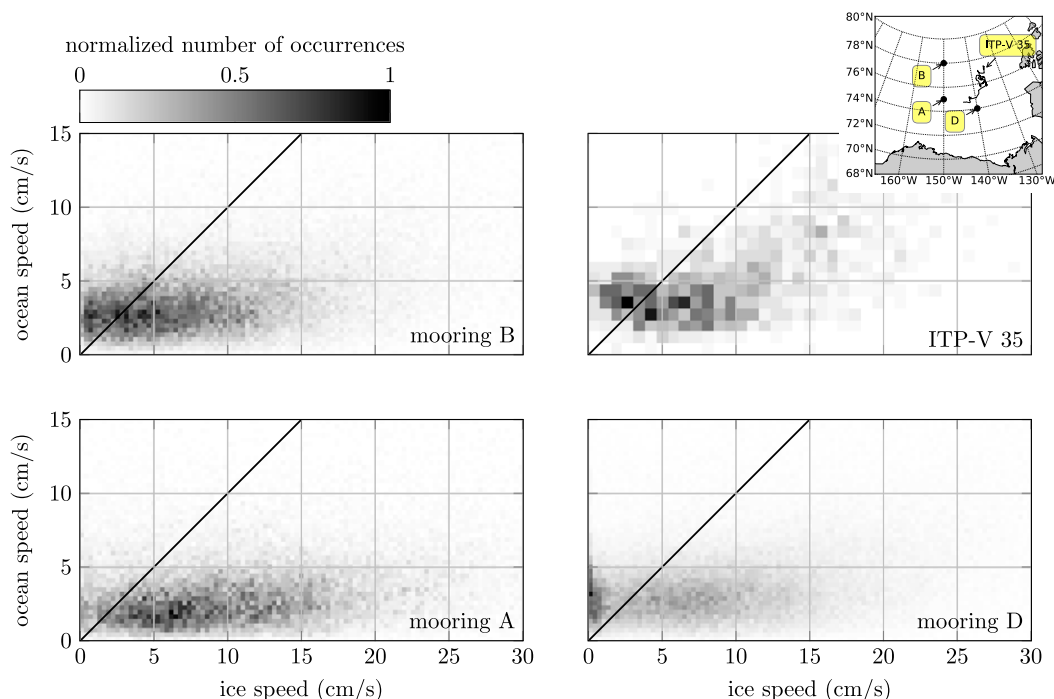


FIG. A1. Ice speed vs ocean speed from ADCP measurement from Beaufort Gyre moorings A, B, and D and from ITP-V35. Ocean speed is averaged over the 5–20-m depth range; points above the black line mark occurrences of the ocean moving faster than the ice and are concentrated at small ice velocities. We remark that ITP-V35 sampled the eastern side of the Beaufort Gyre, where only moderate currents are present. Ocean speeds larger than  $10 \text{ cm}^{-1}$  are a result of the ITP encountering eddies. The top-right map shows the mooring locations and the ITP-V 35 track.

freshwater release by baroclinic instability versus deflation induced by surface ocean–ice frictional processes and to better define the characteristic time scale of the latter. This will be the subject of a follow-up paper.

*Acknowledgments.* We thank Jean-Michel Campin, Edward Dorridge, and James Williams for their help and insights, Jiayan Yang and Thomas Armitage for their suggestions during the review process, and Georgy Manucharyan for his comments. The experiments described here were made possible by support from the NSF program in Arctic Research, Award Number 1603557. The ice-tethered profiler data were collected and made available by the ice-tethered profiler program (Toole et al. 2011; Krishfield et al. 2008) based at the Woods Hole Oceanographic Institution (<http://www.whoi.edu/itp>). Beaufort Gyre mooring data were collected and made available by the Beaufort Gyre Exploration Program based at the Woods Hole Oceanographic Institution (<http://www.whoi.edu/beaufortgyre>) in collaboration with researchers from Fisheries and Oceans Canada at the Institute of Ocean Sciences. (Data are available online at <http://www.whoi.edu/website/beaufortgyre/data>.)

## APPENDIX

### In Situ Measurement of Ice and Ocean Speed

We present in Fig. A1 probability mass plots (normalized) of the ice and ocean current speed from moorings A ( $75^\circ\text{N}$ ,  $150^\circ\text{W}$ ), B ( $78^\circ\text{N}$ ,  $150^\circ\text{W}$ ), and D ( $74^\circ\text{N}$ ,  $140^\circ\text{W}$ ) of the Beaufort Gyre Exploration Project (<http://www.whoi.edu/beaufortgyre/>), together with data from an ITP equipped with a velocity sensor (ITP-V35). Data from ITP-V35, drifting in the eastern Beaufort Sea in the winter of 2009/10, were first presented in Cole et al. (2014), to which we refer the reader for an in-depth description of the data and methods. Current speeds shown in Fig. A1 are averaged over the 5–20-m depth range.

We see that the ocean current speed (vertical axis) is mostly concentrated below  $5 \text{ cm s}^{-1}$ . The ice velocities range between 0 and  $20 \text{ cm s}^{-1}$  or larger and are fastest at mooring A where ice concentrations are lowest (see Fig. 1d). Note that the measured ocean speed can be larger than the ice speed at times (particularly for small ice drift speeds), suggesting that it is not appropriate to neglect the geostrophic velocity in surface stress computations.

## REFERENCES

- Armitage, T. W. K., S. Bacon, A. L. Ridout, S. F. Thomas, Y. Aksenov, and D. J. Wingham, 2016: Arctic sea surface height variability and change from satellite radar altimetry and GRACE, 2003–2014. *J. Geophys. Res. Oceans*, **121**, 4303–4322, <https://doi.org/10.1002/2015JC011579>.
- , —, —, A. A. Petty, S. Wolbach, and M. Tsamados, 2017: Arctic Ocean surface geostrophic circulation 2003–2014. *Cryosphere*, **11**, 1767–1780, <https://doi.org/10.5194/tc-11-1767-2017>.
- Cavalieri, D. J., C. L. Parkinson, P. Gloersen, and H. J. Zwally, 1996: Sea ice concentrations from *Nimbus-7* SMMR and DMSP SSM/I-SSMIS passive microwave data, version 1. NSIDC, accessed 2 April 2017, <https://doi.org/10.5067/8Q08LZQVL0VL>.
- Cole, S. T., M.-L. Timmermans, J. M. Toole, R. A. Krishfield, and F. T. Thwaites, 2014: Ekman veering, internal waves, and turbulence observed under Arctic sea ice. *J. Phys. Oceanogr.*, **44**, 1306–1328, <https://doi.org/10.1175/JPO-D-12-0191.1>.
- Giles, K. A., S. W. Laxon, and A. L. Ridout, 2008: Circumpolar thinning of Arctic sea ice following the 2007 record ice extent minimum. *Geophys. Res. Lett.*, **35**, 2006–2009, <https://doi.org/10.1029/2008GL035710>.
- Kalnay, E., and Coauthors, 1996: The NCEP/NCAR 40-Year Reanalysis Project. *Bull. Amer. Meteor. Soc.*, **77**, 437–471, [https://doi.org/10.1175/1520-0477\(1996\)077<0437:TNYRP>2.0.CO;2](https://doi.org/10.1175/1520-0477(1996)077<0437:TNYRP>2.0.CO;2).
- Krishfield, R., J. Toole, A. Proshutinsky, and M.-L. Timmermans, 2008: Automated ice-tethered profilers for seawater observations under pack ice in all seasons. *J. Atmos. Oceanic Technol.*, **25**, 2091–2105, <https://doi.org/10.1175/2008JTECH0587.1>.
- Kwok, R., G. Spreen, and S. Pang, 2013: Arctic sea ice circulation and drift speed: Decadal trends and ocean currents. *J. Geophys. Res. Oceans*, **118**, 2408–2425, <https://doi.org/10.1002/jgrc.20191>.
- Ma, B., M. Steele, and C. M. Lee, 2017: Ekman circulation in the Arctic Ocean: Beyond the Beaufort Gyre. *J. Geophys. Res. Oceans*, **122**, 3358–3374, <https://doi.org/10.1002/2016JC012624>.
- Manucharyan, G. E., and M. A. Spall, 2016: Wind-driven freshwater buildup and release in the Beaufort Gyre constrained by mesoscale eddies. *Geophys. Res. Lett.*, **43**, 273–282, <https://doi.org/10.1002/2015GL065957>.
- , —, and A. F. Thompson, 2016: A theory of the wind-driven Beaufort Gyre variability. *J. Phys. Oceanogr.*, **46**, 3263–3278, <https://doi.org/10.1175/JPO-D-16-0091.1>.
- , A. F. Thompson, and M. A. Spall, 2017: Eddy memory mode of multidecadal variability in residual-mean ocean circulations with application to the Beaufort Gyre. *J. Phys. Oceanogr.*, **47**, 855–866, <https://doi.org/10.1175/JPO-D-16-0194.1>.
- Martin, T., and R. Gerdes, 2007: Sea ice drift variability in Arctic Ocean Model Intercomparison Project models and observations. *J. Geophys. Res.*, **112**, C04S10, <https://doi.org/10.1029/2006JC003617>.
- , M. Steele, and J. Zhang, 2014: Seasonality and long-term trend of Arctic Ocean surface stress in a model. *J. Geophys. Res. Oceans*, **119**, 1723–1738, <https://doi.org/10.1002/2013JC009425>.
- , M. Tsamados, D. Schroeder, and D. Feltham, 2016: The impact of variable sea ice roughness on changes in Arctic Ocean surface stress: A model study. *J. Geophys. Res. Oceans*, **121**, 1931–1952, <https://doi.org/10.1002/2015JC011186>.
- McPhee, M. G., 2013: Intensification of geostrophic currents in the Canada Basin, Arctic Ocean. *J. Climate*, **26**, 3130–3138, <https://doi.org/10.1175/JCLI-D-12-00289.1>.
- Meneghello, G., J. Marshall, S. T. Cole, and M.-L. Timmermans, 2017: Observational inferences of lateral eddy diffusivity in the halocline of the Beaufort Gyre. *Geophys. Res. Lett.*, **44**, 12 331–12 338, <https://doi.org/10.1002/2017GL075126>.
- Proshutinsky, A., and Coauthors, 2009: Beaufort Gyre freshwater reservoir: State and variability from observations. *J. Geophys. Res.*, **114**, C00A10, <https://doi.org/10.1029/2008JC005104>.
- Simmonds, I., and I. Rudeva, 2012: The Great Arctic Cyclone of August 2012. *Geophys. Res. Lett.*, **39**, L23709, <https://doi.org/10.1029/2012GL054259>.
- Timmermans, M. L., J. Marshall, A. Proshutinsky, and J. Scott, 2017: Seasonally derived components of the Canada Basin halocline. *Geophys. Res. Lett.*, **44**, 5008–5015, <https://doi.org/10.1002/2017GL073042>.
- Toole, J. M., R. A. Krishfield, M.-L. Timmermans, and A. Proshutinsky, 2011: The ice-tethered profiler: Argo of the Arctic. *Oceanography*, **24** (3), 126–135, <https://doi.org/10.5670/oceanog.2011.64>.
- Tschudi, M., C. Fowler, J. S. Maslanik, and W. Meier, 2016: Polar Pathfinder daily 25 km EASE-grid sea ice motion vectors, version 3. NSIDC, accessed 9 March 2017, <https://doi.org/10.5067/O57VAIT2AYYY>.
- Yang, J., 2006: The seasonal variability of the Arctic Ocean Ekman transport and its role in the mixed layer heat and salt fluxes. *J. Climate*, **19**, 5366–5387, <https://doi.org/10.1175/JCLI3892.1>.
- , 2009: Seasonal and interannual variability of downwelling in the Beaufort Sea. *J. Geophys. Res.*, **114**, C00A14, <https://doi.org/10.1029/2008JC005084>.